Simscape Model - Nano Active Stabilization System

Dehaeze Thomas

February 17, 2025

Contents

From last sections:

- Uniaxial: No stiff nano-hexapod (should also demonstrate that here)
- Rotating: No soft nano-hexapod, Decentralized IFF can be used robustly by adding parallel stiffness
- Micro-Station multi body model tuned from a modal analysis
- Multi-body model of a nano-hexapod that can be merged with the multi-body model of the micro-station

In this section:

- Take the model of the nano-hexapod described in previous section (stiffness 1um/N)
- Control kinematics: how the external metrology, the nano-hexapod metrology are used to control the sample's position (Section 1)
- Apply decentralized IFF (Section 2)
- Apply HAC-LAC (Section 3)
  - Check robustness to change of payload and to spindle rotation
  - Simulation of experiments
- Conclusion of the conceptual phase, validation with simulations

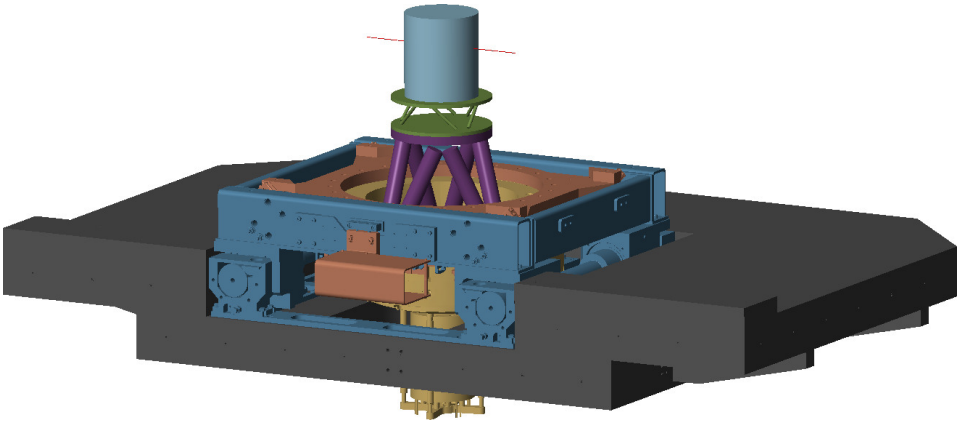

Figure 1: 3D view of the NASS multi-body model

1 Control Kinematics

Figure 1.1 presents a schematic overview of the NASS. This section focuses specifically on the components of the "Instrumentation and Real-Time Control" block.

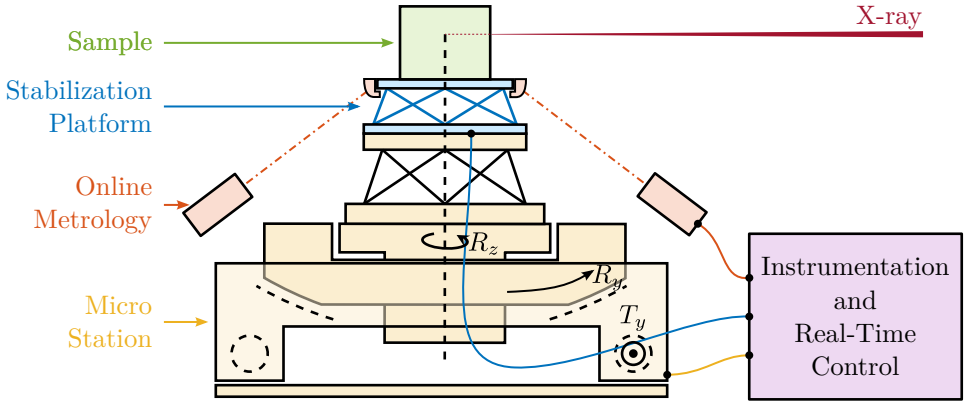

Figure 1.1: Schematic of the Nano Active Stabilization System

As established in the previous section on Stewart platforms, the proposed control strategy combines Decentralized Integral Force Feedback with a High Authority Controller performed in the frame of the struts.

For the Nano Active Stabilization System, computing the positioning errors in the frame of the struts involves three key steps. First, the system computes the desired sample pose relative to a frame representing the point where the X-ray light is focused using micro-station kinematics, as detailed in Section 1.1. Second, it measures the actual sample pose relative to the same fix frame, described in Section 1.2. Finally, it determines the sample pose error and maps these errors to the nano-hexapod struts, as explained in Section 1.3.

The complete control architecture is detailed in Section 1.4.

1.1 Micro Station Kinematics

The micro-station kinematics enables the computation of the desired sample pose from the reference signals of each micro-station stage. These reference signals consist of the desired lateral position r_{D_y}, tilt angle r_{R_y}, and spindle angle r_{R_z}. The micro-hexapod pose is defined by six parameters: three translations $(r_{D_{\mu x}}, r_{D_{\mu y}}, r_{D_{\mu z}})$ and three rotations $(r_{\theta_{\mu x}}, r_{\theta_{\mu y}}, r_{\theta_{\mu z}})$.

Using these reference signals, the desired sample position relative to the fixed frame is expressed through the homogeneous transformation matrix $\boldsymbol{T}_{\mu\text{-station}}$, as defined in equation (1.1).

$$\boldsymbol{T}_{\mu\text{-station}} = \boldsymbol{T}_{D_y} \cdot \boldsymbol{T}_{R_y} \cdot \boldsymbol{T}_{R_z} \cdot \boldsymbol{T}_{\mu\text{-hexapod}} \tag{1.1}$$

$$\begin{aligned}
\boldsymbol{T}_{D_y} &= \begin{bmatrix} 1 & 0 & 0 & 0 \\ 0 & 1 & 0 & r_{D_y} \\ 0 & 0 & 1 & 0 \\ 0 & 0 & 0 & 1 \end{bmatrix} \quad \boldsymbol{T}_{\mu\text{-hexapod}} = \left[\begin{array}{ccc|c} & \boldsymbol{R}_x(r_{\theta_{\mu x}})\boldsymbol{R}_y(r_{\theta_{\mu y}})\boldsymbol{R}_z(r_{\theta_{\mu z}}) & & \begin{matrix} r_{D_{\mu x}} \\ r_{D_{\mu y}} \\ r_{D_{\mu z}} \end{matrix} \\ \hline 0 & 0 & 0 & 1 \end{array}\right] \\
\boldsymbol{T}_{R_z} &= \begin{bmatrix} \cos(r_{R_z}) & -\sin(r_{R_z}) & 0 & 0 \\ \sin(r_{R_z}) & \cos(r_{R_z}) & 0 & 0 \\ 0 & 0 & 1 & 0 \\ 0 & 0 & 0 & 1 \end{bmatrix} \quad \boldsymbol{T}_{R_y} = \begin{bmatrix} \cos(r_{R_y}) & 0 & \sin(r_{R_y}) & 0 \\ 0 & 1 & 0 & 0 \\ -\sin(r_{R_y}) & 0 & \cos(r_{R_y}) & 0 \\ 0 & 0 & 0 & 1 \end{bmatrix}
\end{aligned} \tag{1.2}$$

1.2 Computation of the sample's pose error

The external metrology system measures the sample position relative to the fixed granite. Due to the system's symmetry, this metrology provides measurements for five degrees of freedom: three translations (D_x, D_y, D_z) and two rotations (R_x, R_y).

The sixth degree of freedom (R_z) is still required to compute the errors in the frame of the nano-hexapod struts (i.e. to compute the nano-hexapod inverse kinematics). This R_z rotation is estimated by combining measurements from the spindle encoder and the nano-hexapod's internal metrology, which consists of relative motion sensors in each strut (note that the micro-hexapod is not used for R_z rotation, and is therefore ignore for R_z estimation).

The measured sample pose is represented by the homogeneous transformation matrix $\boldsymbol{T}_{\text{sample}}$, as shown in equation (1.3).

$$\boldsymbol{T}_{\text{sample}} = \left[\begin{array}{ccc|c} & \boldsymbol{R}_x(R_x)\boldsymbol{R}_y(R_y)\boldsymbol{R}_z(R_z) & & \begin{matrix} D_x \\ D_y \\ D_z \end{matrix} \\ \hline 0 & 0 & 0 & 1 \end{array}\right] \tag{1.3}$$

1.3 Position error in the frame of the struts

The homogeneous transformation formalism enables straightforward computation of the sample position error. This computation involves the previously computed homogeneous 4×4 matrices: $\boldsymbol{T}_{\mu\text{-station}}$ representing the desired pose, and $\boldsymbol{T}_{\text{sample}}$ representing the measured pose. Their combination yields $\boldsymbol{T}_{\text{error}}$, which expresses the position error of the sample in the frame of the rotating nano-hexapod, as shown in equation (1.4).

$$\boldsymbol{T}_{\text{error}} = \boldsymbol{T}_{\mu\text{-station}}^{-1} \cdot \boldsymbol{T}_{\text{sample}} \tag{1.4}$$

The known structure of the homogeneous transformation matrix facilitates efficient real-time computation of the inverse. From $\boldsymbol{T}_{\text{error}}$, the position and orientation errors $\boldsymbol{\epsilon}_{\mathcal{X}} = [\epsilon_{D_x},\ \epsilon_{D_y},\ \epsilon_{D_z},\ \epsilon_{R_x},\ \epsilon_{R_y},\ \epsilon_{R_z}]$ of the sample are extracted using equation (1.5):

$$
\begin{aligned}
\epsilon_{D_x} &= \boldsymbol{T}_{\text{error}}(1,4) \\
\epsilon_{D_y} &= \boldsymbol{T}_{\text{error}}(2,4) \\
\epsilon_{D_z} &= \boldsymbol{T}_{\text{error}}(3,4) \\
\epsilon_{R_y} &= \text{atan2}(\boldsymbol{T}_{\text{error}}(1,3), \sqrt{\boldsymbol{T}_{\text{error}}(1,1)^2 + \boldsymbol{T}_{\text{error}}(1,2)^2}) \\
\epsilon_{R_x} &= \text{atan2}(-\boldsymbol{T}_{\text{error}}(2,3)/\cos(\epsilon_{R_y}), \boldsymbol{T}_{\text{error}}(3,3)/\cos(\epsilon_{R_y})) \\
\epsilon_{R_z} &= \text{atan2}(-\boldsymbol{T}_{\text{error}}(1,2)/\cos(\epsilon_{R_y}), \boldsymbol{T}_{\text{error}}(1,1)/\cos(\epsilon_{R_y}))
\end{aligned}
\tag{1.5}
$$

Finally, these errors are mapped to the strut space through the nano-hexapod Jacobian matrix (1.6).

$$
\boldsymbol{\epsilon}_{\mathcal{L}} = \boldsymbol{J} \cdot \boldsymbol{\epsilon}_{\mathcal{X}} \tag{1.6}
$$

1.4 Control Architecture - Summary

The complete control architecture is summarized in Figure 1.2. The sample pose is measured using external metrology for five degrees of freedom, while the sixth degree of freedom (Rz) is estimated by combining measurements from the nano-hexapod encoders and spindle encoder.

The sample reference pose is determined by the reference signals of the translation stage, tilt stage, spindle, and micro-hexapod. Position error computation follows a two-step process: first, homogeneous transformation matrices are used to determine the error in the nano-hexapod frame, then the Jacobian matrix $\boldsymbol{J}$ maps these errors to individual strut coordinates.

For control purposes, force sensors mounted on each strut are used in a decentralized way for active damping, as detailed in Section 2. Then, the high authority controller uses the computed errors in the frame of the struts to provides real-time stabilization of the sample position (Section 3).

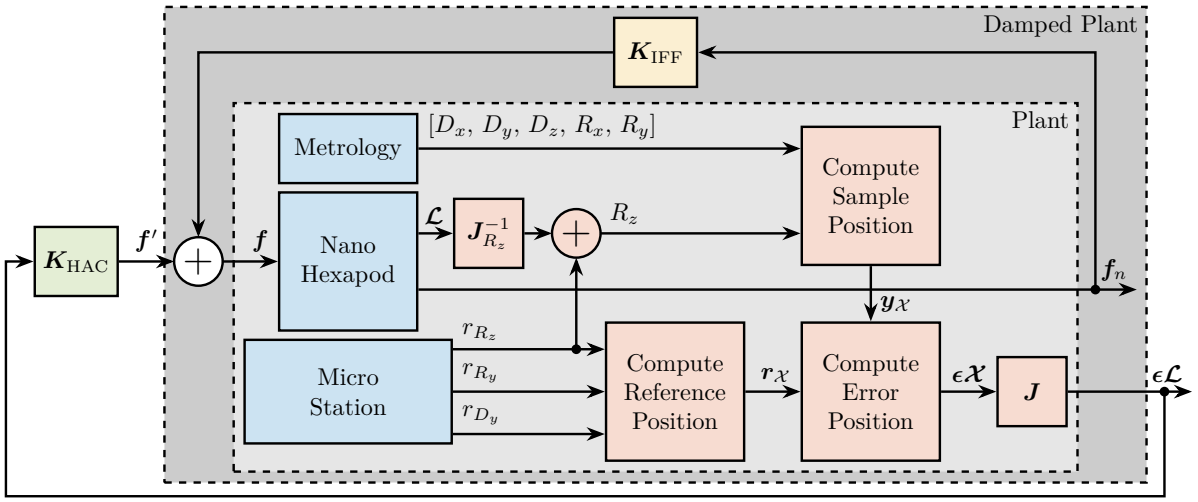

Figure 1.2: The physical systems are shown in blue, the control kinematics in red, the decentralized Integral Force Feedback in yellow and the centralized High Authority Controller in green.

2 Decentralized Active Damping

Building upon the uniaxial model study, this section implements decentralized Integral Force Feedback (IFF) as the first component of the HAC-LAC strategy. Springs in parallel to the force sensors are used to guarantee the control robustness as was found using the 3DoF rotating model. The objective here is to design a decentralized IFF controller that provides good damping of the nano-hexapod modes across payload masses ranging from 1 to 50 kg and rotational velocity up to 360 deg/s. Used payloads have a cylindrical shape with 250 mm height and with masses of 1 kg, 25 kg, and 50 kg.

2.1 IFF Plant

Transfer functions from actuator forces f_i to force sensor measurements f_{mi} are computed using the multi-body model. Figure 2.1 examines how parallel stiffness affects the plant dynamics, with identification performed at maximum spindle velocity $\Omega_z = 360\,\text{deg/s}$ and with a payload mass of 25 kg.

Without parallel stiffness (Figure 2.1a), the dynamics exhibits non-minimum phase zeros at low frequency, confirming predictions from the three-degree-of-freedom rotating model. Adding parallel stiffness (Figure 2.1b) transforms these into minimum phase complex conjugate zeros, enabling unconditionally stable decentralized IFF implementation.

Though both cases show significant coupling around resonances, stability is guaranteed by the collocated arrangement of actuators and sensors **preumont08˙trans˙zeros˙struc˙contr˙with**.

The effect of rotation, shown in Figure 2.2a, is negligible as the actuator stiffness ($k_a = 1\,N/\mu m$) is large compared to the negative stiffness induced by gyroscopic effects (estimated from the 3DoF rotating model).

Figure 2.2b illustrate the effect of payload mass on the plant dynamics. While the poles and zeros are shifting with payload mass, the alternating pattern of poles and zeros is maintained, ensuring that the phase remains bounded between 0 and 180 degrees, and thus good robustness properties.

2.2 Controller Design

Previous analysis using the 3DoF rotating model showed that decentralized Integral Force Feedback (IFF) with pure integrators is unstable due to gyroscopic effects caused by spindle rotation. This finding is also confirmed with the multi-body model of the NASS: the system is unstable when using pure integrators and without parallel stiffness.

This instability can be mitigated by introducing sufficient stiffness in parallel with the force sensors. However, as illustrated in Figure 2.1b, adding parallel stiffness increases the low frequency gain. If

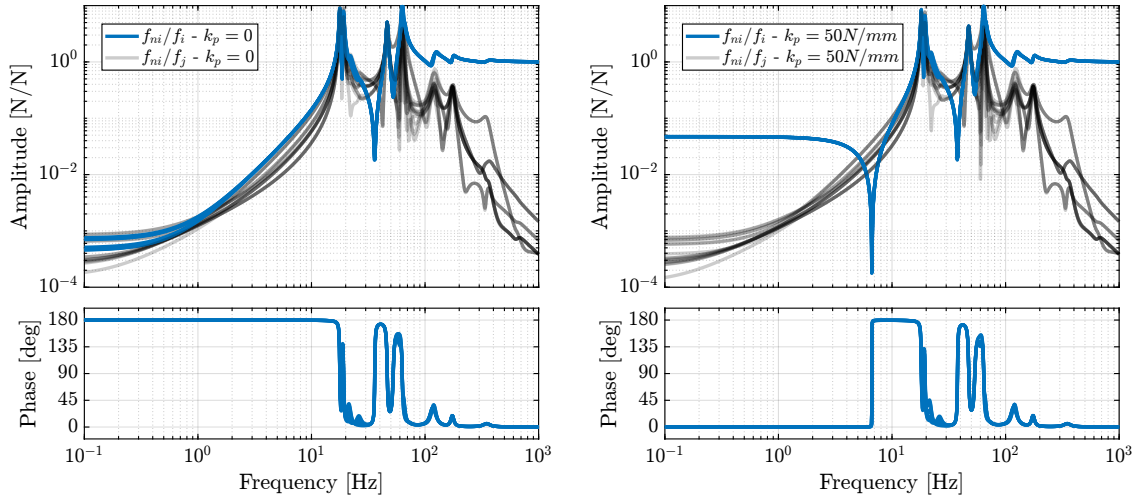

(a) without parallel stiffness

(b) with parallel stiffness

Figure 2.1: Effect of stiffness parallel to the force sensor on the IFF plant with $\Omega_z = 360\,\text{deg/s}$ and payload mass of 25kg. The dynamics without parallel stiffness has non-minimum phase zeros at low frequency (a). The added parallel stiffness transforms the non-minimum phase zeros to complex conjugate zeros (b)

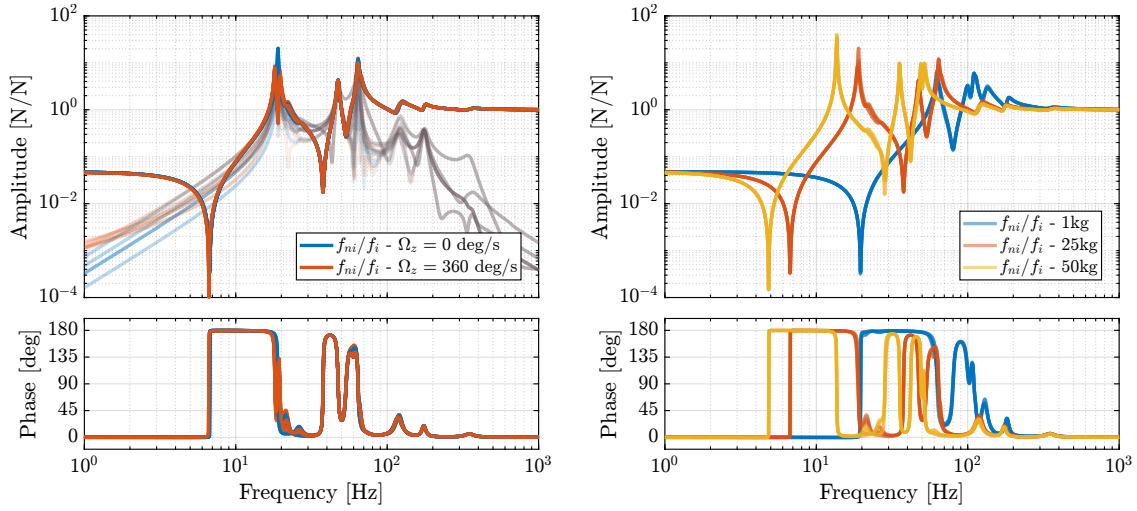

(a) Effect of Spindle rotation

(b) Effect of payload mass

Figure 2.2: Effect of the Spindle's rotational velocity on the IFF plant (a) and effect of the payload's mass on the IFF plant (b)

using pure integrators, this would results in high loop gain at low frequencies, adversely affecting the damped plant dynamics, which is undesirable. To resolve this issue, a second-order high-pass filter is introduced to limit the low frequency gain, as shown in Equation (2.1).

$$\boldsymbol{K}_{\text{IFF}}(s) = g \cdot \begin{bmatrix} K_{\text{IFF}}(s) & & 0 \\ & \ddots & \\ 0 & & K_{\text{IFF}}(s) \end{bmatrix}, \quad K_{\text{IFF}}(s) = \frac{1}{s} \cdot \frac{\frac{s^2}{\omega_z^2}}{\frac{s^2}{\omega_z^2} + 2\xi_z \frac{s}{\omega_z} + 1} \tag{2.1}$$

The cut-off frequency of the second-order high-pass filter is tuned to be below the frequency of the complex conjugate zero for the highest mass, which is at 5 Hz. The overall gain is then increased to have large loop gain around resonances to be damped, as illustrated in Figure 2.3.

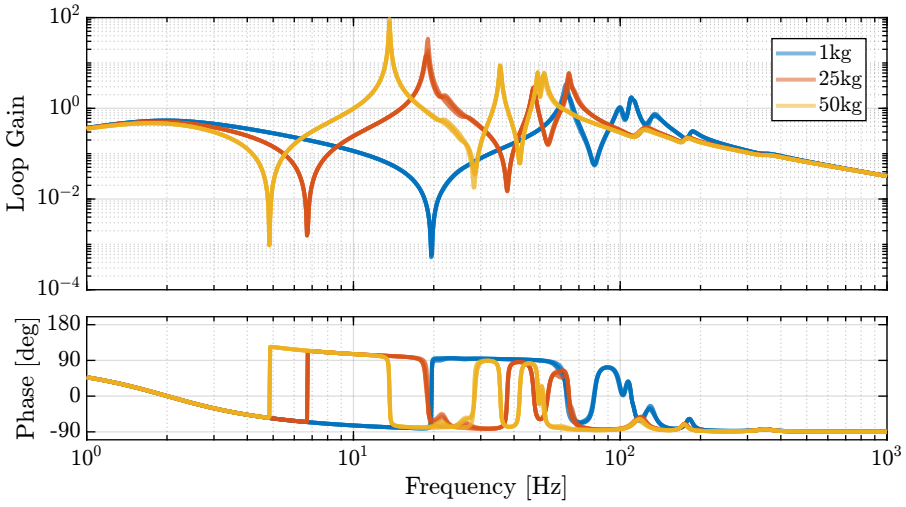

Figure 2.3: Loop gain for the decentralized IFF: $K_{\text{IFF}}(s) \cdot \frac{f_{mi}}{f_i}(s)$

To verify stability, root loci for the three payload configurations are computed and shown in Figure 2.4. The results demonstrate that the closed-loop poles remain within the left-half plane, indicating the robust stability properties of the applied decentralized IFF.

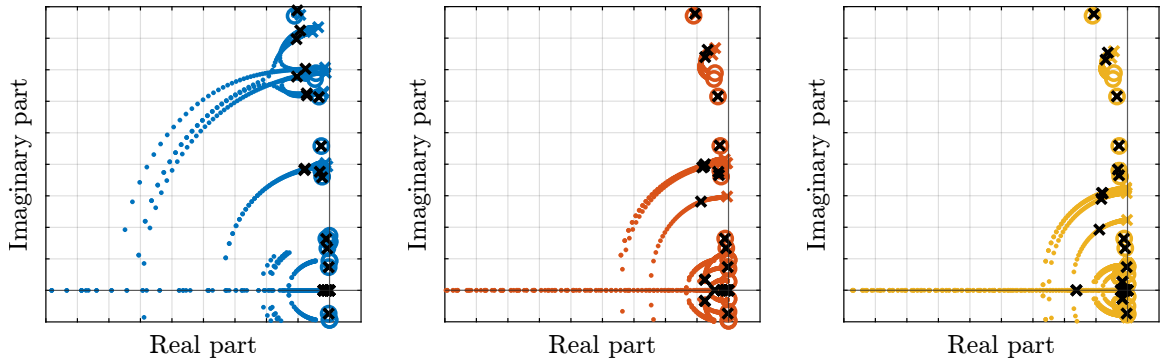

(a) 1 kg **(b)** 25 kg **(c)** 50 kg

Figure 2.4: Root Loci for Decentralized IFF for three payload masses. Closed-loop poles are shown by the black crosses.

3 Centralized Active Vibration Control

Effect of micro-station compliance Compare plant with “rigid” u-station and normal u-station

- Effect of IFF
- Effect of payload mass
- Decoupled plant
- Controller design

From control kinematics:

- Talk about issue of not estimating Rz from external metrology? (maybe could be nice to discuss that during the experiments!)
- Show what happens is Rz is not estimated (for instance supposed equaled to zero =¿ increased coupling)

3.1 HAC Plant

- Effect of rotation: 3.1a Add some coupling at low frequency, but still small at the considered velocity. This is thanks to the relatively stiff nano-hexapod (CF rotating model)
- Effect of payload mass: Decrease resonance frequencies Increase coupling: 3.1b =¿ control challenge for high payload masses
- Other effects such as: Ry tilt angle, Rz spindle position, micro-hexapod position are found to have negligible effect on the plant dynamics. This is thanks to the fact the the plant dynamics is well decoupled from the micro-station dynamics.
- Effect of IFF on the plant 3.2a Modes are well damped Small coupling increase at low frequency
- Benefits of using IFF 3.2b with added damping, the set of plants to be controlled (with payloads from 1kg to 50kg) is more easily controlled. Between 10 and 50Hz, the plant dynamics does not vary a lot with the frequency, whereas without active damping, it would be impossible to design a robust controller with bandwidth above 10Hz that is robust to the change of payload

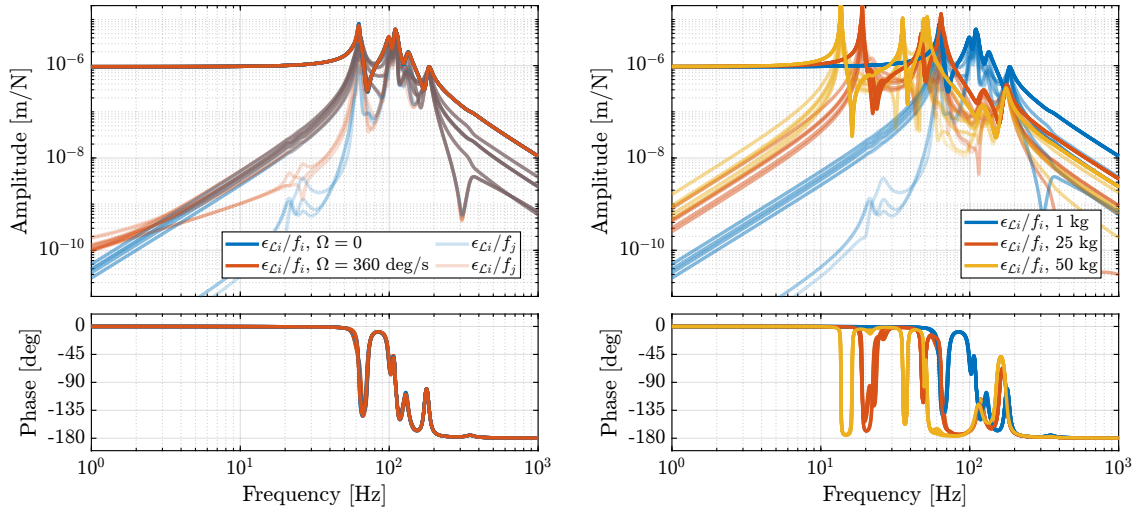

(a) Effect of rotational velocity Ω_z

(b) Effect of payload's mass

Figure 3.1: Effect of the Spindle's rotational velocity on the positioning plant (a) and effect of the payload's mass on the positioning plant (b)

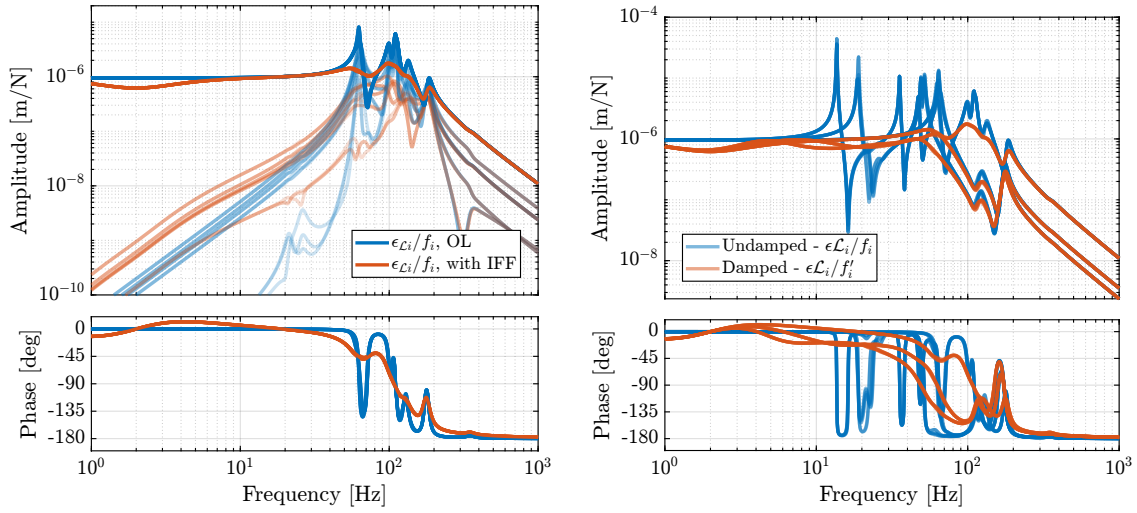

(a) Effect of IFF - $m = 1\,\text{kg}$

(b) Effect of IFF on the set of plants to control

Figure 3.2: Effect of the Spindle's rotational velocity on the positioning plant (a) and effect of the payload's mass on the positioning plant (b)

3.2 Effect of micro-station compliance

Micro-Station complex dynamics has almost no effect on the plant dynamics (Figure 3.3):

- adds some alternating poles and zeros above 100Hz, which should not be an issue for control

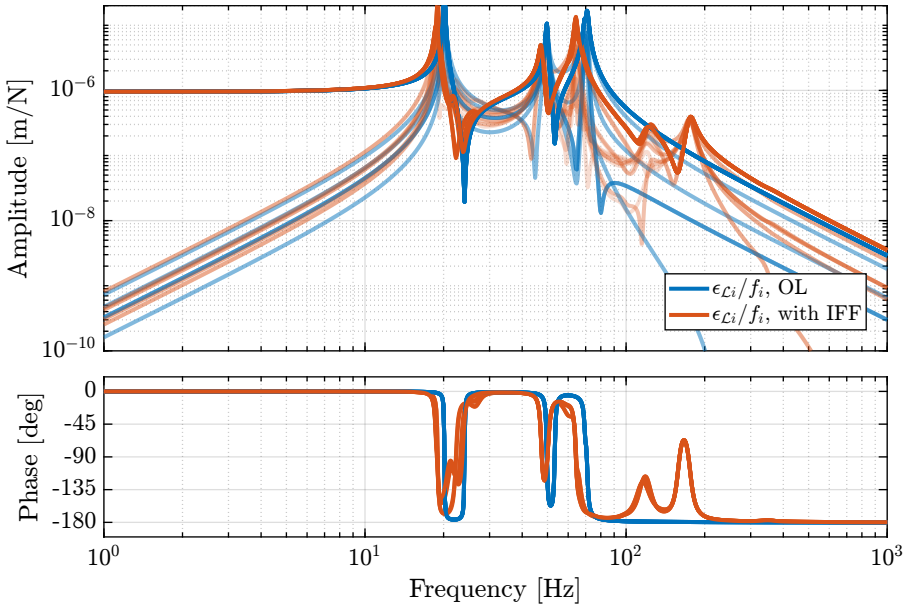

Figure 3.3: Effect of the micro-station limited compliance on the plant dynamics

3.3 Higher or lower nano-hexapod stiffness?

Goal: confirm the analysis with simpler models (uniaxial and 3DoF) that a nano-hexapod stiffness of $\approx 1\,N/\mu m$ should give better performances than a very stiff or very soft nano-hexapod.

- **Stiff nano-hexapod**: uniaxial model: high nano-hexapod stiffness induce coupling between the nano-hexapod and the micro-station dynamics. considering the complex dynamics of the micro-station as shown by the modal analysis, that would result in a complex system to control To show that, a nano-hexapod with actuator stiffness equal to 100N/um is initialized, payload of 25kg. The dynamics from $\boldsymbol{f}$ to $\boldsymbol{\epsilon_{\mathcal{L}}}$ is identified and compared to the case where the micro-station is infinitely rigid (figure 3.4a):
  - Coupling induced by the micro-station: much more complex and difficult to model / predict
  - Similar to what was predicted using the uniaxial model
- **Soft nano-hexapod**: Nano-hexapod with stiffness of 0.01N/um is initialized, payload of 25kg. Dynamics is identified with no spindle rotation, and with spindle rotation of 36deg/s and 360deg/s (Figure 3.4b)
  - Rotation as huge effect on the dynamics: unstable for high rotational velocities, added

coupling due to gyroscopic effects, and change of resonance frequencies as a function of the rotational velocity

– Simple 3DoF rotating model is helpful to understand the complex effect of the rotation =¿ similar conclusion

– Say that controlling the frame of the struts is not adapted with a soft nano-hexapod, but we should rather control in the frame matching the center of mass of the payload, but we would still obtain large coupling and change of dynamics due to gyroscopic effects.

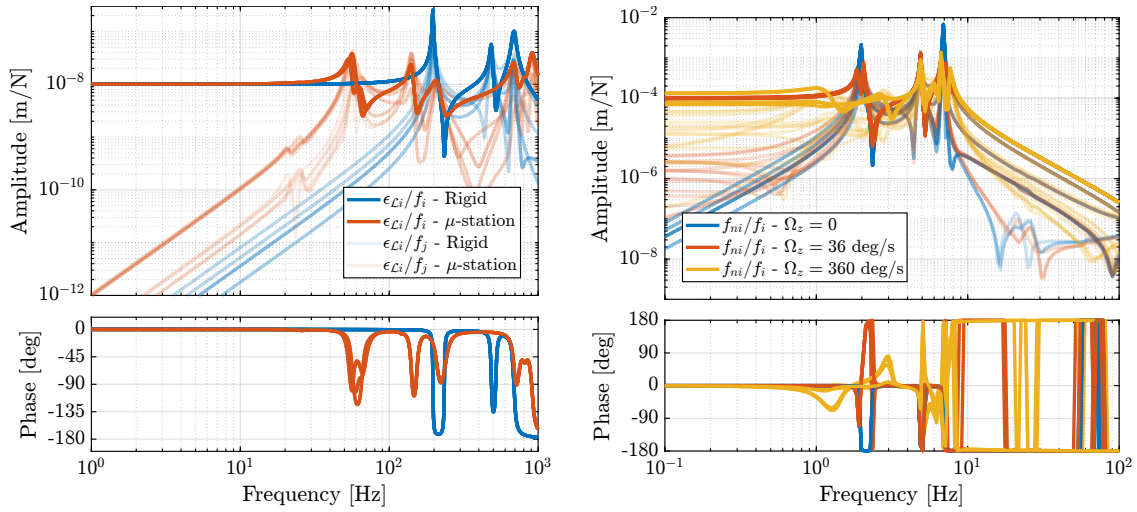

(a) Stiff nano-hexapod - Coupling with the micro-station

(b) Soft nano-hexapod - Effect of Spindle rotational velocity

Figure 3.4: Plant dynamics of a stiff ($k_a = 100\,N/\mu m$) nano-hexapod (a) and of a soft ($k_a = 0.01\,N/\mu m$) nano-hexapod (b)

3.4 Controller design

In this section, a high authority controller is design such that:

- it is robust to the change of payload mass (i.e. is should be stable for all the damped plants of Figure 3.2b)
- it has reasonably high bandwidth to give good performances (here 10Hz)

(3.1)

$$K_{\text{HAC}}(s) = g_0 \cdot \underbrace{\frac{\omega_c}{s}}_{\text{int}} \cdot \underbrace{\frac{1}{\sqrt{\alpha}} \frac{1 + \frac{s}{\omega_c/\sqrt{\alpha}}}{1 + \frac{s}{\omega_c\sqrt{\alpha}}}}_{\text{lead}} \cdot \underbrace{\frac{1}{1 + \frac{s}{\omega_0}}}_{\text{LPF}}, \quad (\omega_c = 2\pi 10\,\text{rad/s},\ \alpha = 2,\ \omega_0 = 2\pi 80\,\text{rad/s}) \tag{3.1}$$

- "Decentralized" Loop Gain: Bandwidth around 10Hz
- Characteristic Loci: Stable for all payloads with acceptable stability margins

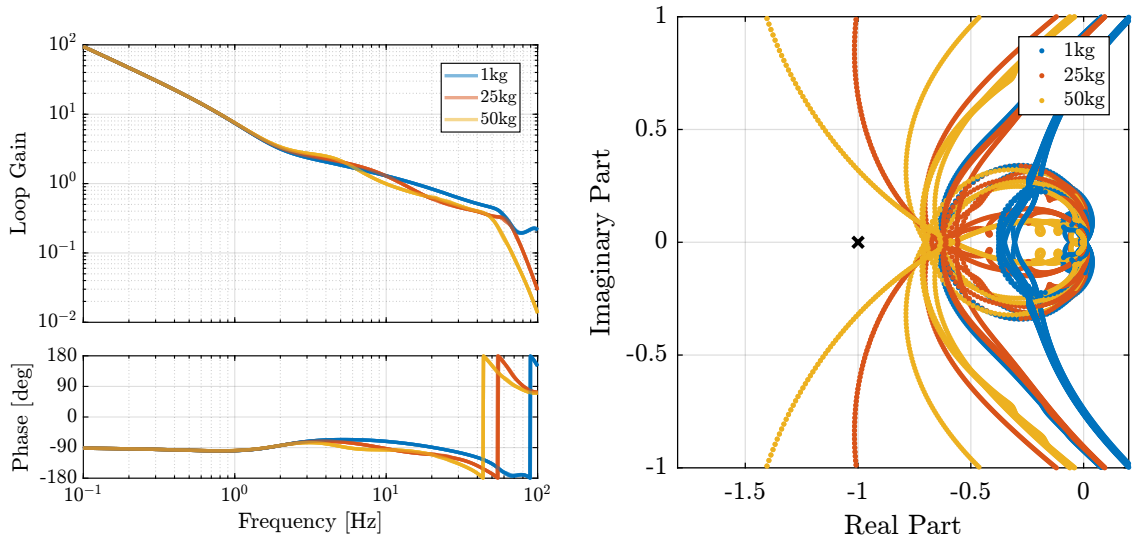

(a) Loop Gain **(b)** Characteristic Loci

Figure 3.5: High Authority Controller - "Diagonal Loop Gain" (a) and Characteristic Loci (b)

3.5 Tomography experiment

- Validation of concept with tomography scans at the highest rotational velocity of $\Omega_z = 360\,\mathrm{deg/s}$
- Compare obtained results with the smallest beam size that is expected with future beamline upgrade: 200nm (horizontal size) x 100nm (vertical size)
- Take into account the two main sources of disturbances: ground motion, spindle vibrations Other noise sources are not taken into account here as they will be optimized latter (detail design phase): measurement noise, electrical noise for DAC and voltage amplifiers, ...

The open-loop errors and the closed-loop errors for the tomography scan with the light sample $1\,kg$ are shown in Figure 3.6.

- Effect of payload mass (Figure 3.7): Worse performance for high masses, as expected from the control analysis, but still acceptable considering that the rotational velocity of 360deg/s is only used for light payloads.

Conclusion

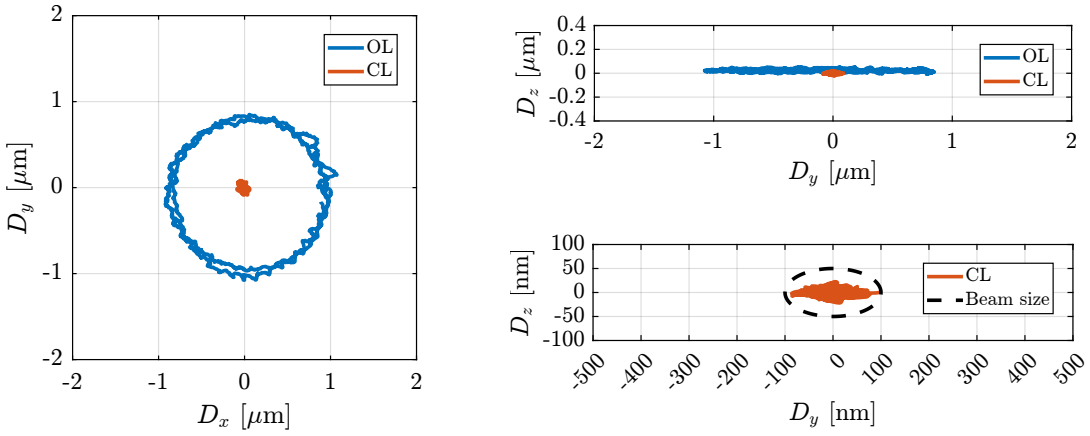

(a) XY plane **(b)** YZ plane

Figure 3.6: Position error of the sample in the XY (a) and YZ (b) planes during a simulation of a tomography experiment at 360 deg/s. 1kg payload is placed on top of the nano-hexapod.

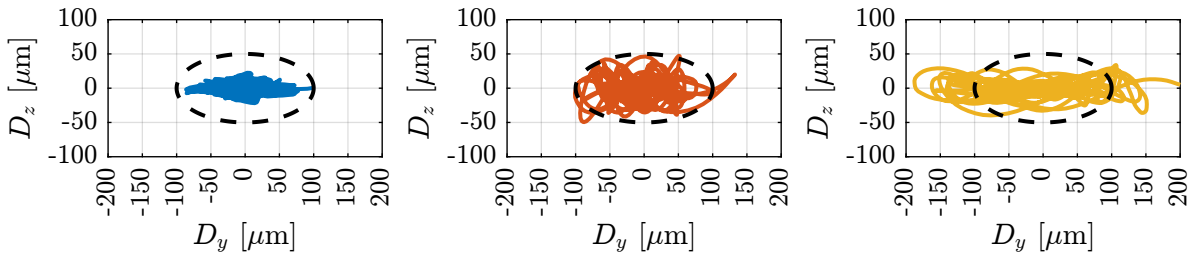

(a) $m = 1\,kg$ **(b)** $m = 25\,kg$ **(c)** $m = 50\,kg$

Figure 3.7: Simulation of tomography experiments - 360deg/s. Beam size shown by dashed black

Conclusion